1-1-2020

Comparison of resting-state functional connectivity in marmosets with tracer-based cellular connectivity

Yuki Hori
Robarts Research Institute

David J. Schaeffer
Robarts Research Institute

Kyle M. Gilbert
Robarts Research Institute

Lauren K. Hayrynen
Robarts Research Institute

Justine C. Cléry
Robarts Research Institute

See next page for additional authors

Authors

Yuki Hori, David J. Schaeffer, Kyle M. Gilbert, Lauren K. Hayrynen, Justine C. Cléry, Joseph S. Gati, Ravi S. Menon, and Stefan Everling

Comparison of resting-state functional connectivity in marmosets with tracer-based cellular connectivity

Yuki Hori [a], David J. Schaeffer [a], Kyle M. Gilbert [a], Lauren K. Hayrynen [a], Justine C. Cléry [a], Joseph S. Gati [a], Ravi S. Menon [a], Stefan Everling [a, b, *]

[a] Centre for Functional and Metabolic Mapping, Robarts Research Institute, The University of Western Ontario, London, Ontario, N6A 5B7, Canada
[b] Department of Physiology and Pharmacology, The University of Western Ontario, London, Ontario, N6A 5C1, Canada

ARTICLE INFO

ABSTRACT

Resting-state functional MRI (RS-fMRI) is widely used to assess how strongly different brain areas are connected. However, this connection obtained by RS-fMRI, which is called functional connectivity (FC), simply refers to the correlation of blood oxygen level-dependent (BOLD) signals across time it has yet to be quantified how accurately FC reflects cellular connectivity (CC). In this study, we elucidated this relationship using RS-fMRI and quantitative tracer data in marmosets. In addition, we also elucidated the effects of distance between two brain regions on the relationship between FC and CC across seed region. To calculate FC, we used full correlation approach that is considered to reflect not only direct (monosynaptic connections) but also indirect pathways (polysynaptic connections). Our main findings are that: (1) overall FC obtained by RS-fMRI was highly correlated with tracer-based CC, but correlation coefficients varied remarkably across seed regions; (2) the strength of FC decreased with increase in the distance between two regions; (3) correlation coefficients between FC and CC after regressing out the effects of the distance between two regions still varied across seed regions, but some regions have strong correlations. These findings suggest that although FC reflects the strength of monosynaptic pathways, it is strongly affected by the distance between regions.

1. Introduction

Resting-state functional magnetic resonance imaging (RS-fMRI) is widely used to infer how strongly different brain areas are connected (Damoiseaux and Greicius, 2009; Fox and Raichle, 2007; Johnston et al., 2008; Park and Friston, 2013; Smith et al., 2013; Sporns, 2013), and how these connections are altered as a function of various neuropathologies (Greicius et al., 2004; Helmich et al., 2010; Rombouts et al., 2005; Rytty et al., 2013; Wang et al., 2006; Wu et al., 2009; Zarei et al., 2013; Zhou et al., 2010). However, canonically derived functional connectivity (FC) between two brain areas simply refers to the correlation of blood oxygen level-dependent (BOLD) signals across time (i.e., with no information about the underlying axons and synapses responsible for connections). Thus, it is still unclear how accurately FC reflects anatomical connectivity, as mediated by the presence of axonal connections between the two areas.

Non-invasive diffusion tractography and invasive chemical or viral tracing techniques are widely used to detect anatomical connectivity.

The relationship between RS-fMRI-based FC and anatomical connectivity in humans has been assessed using diffusion-based tractography (Damoiseaux and Greicius, 2009; Greicius et al., 2009; Hagmann et al., 2008; Honey et al., 2009; Koch et al., 2002; Skudlarski et al., 2008; Van den Heuvel et al., 2008). The first study that compared FC with structural connectivity (SC) obtained by diffusion tractography (Koch et al., 2002), found positive correlations between FC and SC only along the central sulcus. Following the growing interest and techniques of RS-fMRI, several studies revealed more details about the relationship between FC and SC. Two groups focused on the correspondence between SC and FC within the default mode network (Greicius et al., 2009; Van den Heuvel et al., 2008) and one group assessed the relationship between SC and FC at single voxel levels (Skudlarski et al., 2008). These studies concluded that although FC reflects SC to some extent, the precise relationship is unknown. Soon afterwards, Honey et al. reported that whereas strong SC is robustly related to FC, the presence of FC does not automatically imply SC (Honey et al., 2009). The authors also showed that a part of FC without directional linkage can be accounted for by indirect

---

anatomical connection (polysynaptic connection). Although very valuable for many purposes, diffusion-based tractography is an indirect method for assessing SC with its own problems (Shen et al., 2019), particularly its difficulty to resolve crossing fibers (Jbabdi et al., 2015; Jbabdi and Johansen-Berg, 2011).

The gold standard for directly identifying monosynaptic axonal pathways is the chemical tracer technique that require ex-vivo tissue processing (Abe et al., 2018; Burman et al., 2015; Majka et al., 2016; Reser et al., 2017, 2013; Swanson, 1982; Warner et al., 2015; Zeater et al., 2019) and thus can only be used in animal models. Non-human primates are the most appropriate model because of their close phylogenetic relationship to humans and their similar brain organization (Pozzi et al., 2014; Van Essen and Dierker, 2007). To date, only two studies have investigated the relationship between FC and tracer-based cellar connectivity (CC) in Old-World macaque monkeys (Miranda-Dominguez et al., 2014; Shen et al., 2012). Shen et al. compared FC with CC derived from the CoCoMac database (Stephan et al., 2001). However, this database contains the qualitative (no, weak, moderate, and strong) CC of 82 cortical regions rather than quantitative CC (e.g. the fraction of extrinsic labeled neurons). In addition, different nomenclatures of the areas are used because data was collected by multiple institutes, making the comparability of the injections sites ambiguous in some cases. Miranda-Dominguez and colleagues investigated the relationship between FC and quantitative CC derived from a retrograde tracer study of 29 cortical areas in one hemisphere in macaques (Markov et al., 2014). This study focused on an interspecies comparison of the structure-function relationship between humans and macaques and did not consider the effects of the distance between two brain regions on FC, even though FC is affected by the distance. Thus, there is no direct comparisons of RS-fMRI FC with quantitative tracer data that investigated the effects of the distance between brain regions on FC.

Here we used New World common marmoset monkeys (*Callithrix jacchus*) to address two long-standing questions about the relationship between FC and CC: (1) how accurately does FC measured by RS-fMRI reflect tracer-based CC; (2) does the FC reflect the strength of CC after regressing out the effects of the distance between brain regions. For this purpose, the Marmoset Brain Connectivity Atlas (www.marmoset brain.org) (Majka et al., 2016) provides an extensive quantitative database of retrograde tracer data (i.e., tracer connection strength is included) in these monkeys, and the marmoset's small size is ideal for ultra-high field small-bore fMRI, affording high spatial resolution and signal-to-noise ratio (SNR).

2. Methods

2.1. MRI data acquisition

All experimental procedures were in accordance with the Canadian Council of Animal Care policy and a protocol approved by the Animal Care Committee of the University of Western Ontario Council on Animal Care. Nine marmosets (four females), whose weight ranged from 263 g to 480 g (mean ± standard deviation: 372 ± 63 g) and ages ranged from 1.0 year to 6.0 years old (mean ± standard deviation: 2.9 ± 1.9 years old), were used in this study.

The marmosets were head-fixed in the stereotaxic position using a custom-built MRI bed with ear bars and a palate bar housed within the anesthesia mask (design details and computer-aided design (CAD) files are available in Schaeffer et al., 2019c). They were initially sedated with an intramuscular injection of ketamine (20 mg/kg). After an animal was positioned in an animal holder, anesthesia was maintained using the inhalation of 1.5% isoflurane with a mixture of oxygen (1.75–2.25 l/min) through the mask. During scans, a veterinary technician monitored respiration rate, SpO_2 and heart rate via a pulse oximeter and observed these values to be within a normal range throughout scans. Body temperature was measured and maintained using warm-water circulating blankets, thermal insulation and warmed air.

Data were acquired using an 9.4-T, 31-cm horizontal bore magnet (Varian/Agilent, Yarnton, UK) and Bruker BioSpec Avance III console with the software package Paravision-6 (Bruker BioSpin Corp, Billerica, MA), a custom-built high-performance 15-cm-diameter gradient coil with 400-mT/m maximum gradient strength (Peterson et al., 2018), and the 8-channel phased array receive coil (Gilbert et al., 2017). Radiofrequency transmission was accomplished with a quadrature birdcage coil (12-cm inner diameter) built in-house. All imaging was performed at the Centre for Functional and Metabolic Mapping at the University of Western Ontario. Functional images were acquired with 4–6 functional runs (at 600 vol each) for each animal, using gradient-echo based single-shot echo-planar imaging sequence with the following parameters: TR = 1500 ms, TE = 15 ms, flip angle = 40°, field of view (FOV) = 64 × 64 mm, matrix size = 128 × 128, voxel size = 0.5 mm isotropic, slices = 42, bandwidth = 500 kHz, generalized autocalibrating parallel acquisition (GRAPPA) acceleration factor (anterior-posterior) = 2. A T2-weighted (T2w) image was acquired for each animal using rapid imaging with refocused echoes (RARE) sequences with the following parameters: TR = 5500 ms, TE = 53 ms, FOV = 51.2 × 51.2 mm, matrix size = 384 × 384, voxel size = 0.133 × 0.133 × 0.5 mm, slices = 42, bandwidth = 50 kHz, GRAPPA acceleration factor (anterior-posterior) = 2.

2.2. Image preprocessing

Data was preprocessed using FSL software (Smith et al., 2004). Raw MRI images were first converted to Neuro Informatics Technology Initiative (NIfTI) format (Li et al., 2016) and reoriented from the sphinx position. A brain mask was created using FSL tools and National Institutes of Health (NIH) T2w brain template (Liu et al., 2018), which has only the brain (as it is *ex vivo*, without a skull). The brain region was first roughly identified from individual T2w images using the brain extraction tool (BET) with the following options: radius of 25–35 mm and fractional intensity threshold of 0.3. The NIH T2w brain template (Liu et al., 2018) was then linearly and non-linearly registered to individual brain images using FMRIB's linear registration tool (FLIRT) and FMRIB's nonlinear registration tool (FNIRT) to more accurately create the brain mask. Brain images were then extracted using the brain mask and normalized to the NIH template using FLIRT and FNIRT. RS-fMRI images were corrected for motion using FLIRT and registered to the T2w image using FLIRT. Principal component analysis (PCA) was applied to remove the unstructured noise from RS-fMRI time courses, followed by independent component analysis (ICA) with the decomposition number of 200 using the Multivariate Exploratory Linear Optimized Decomposition into Independent Components (MELODIC) module of the FSL software package. The obtained components were classified as signal or noise such as eye movement, cerebral spinal flow pulsation, heart rate and respiratory artifacts based on the criteria as shown in a previous report (Griffanti et al., 2017), and noise components were regressed out from the RS-fMRI time course using the FSL tool (fsl_regfilt). All RS-fMRI images were normalized to the NIH template using RS-fMRI-to-T2w and T2w-to-template transformation matrices, followed by spatial smoothing by a Gaussian kernel with full width of half maximum value of 1.0 mm.

2.3. Calculation of functional connectivity

After preprocessing, full correlation coefficient were calculated as a index of FC. All RS-fMRI images were concatenated and parcellated into 139 regions using the Connectome Workbench (Marcus et al., 2011) and volumes of interest (VOIs) based on the Paxinos Atlas (Liu et al., 2018; Paxinos et al., 2012). The VOIs used here were supplied by the NITRC website (Liu et al., 2018) and modified to integrate left and right regions (116 cortical regions and 23 subcortical regions). Abbreviations and locations of brain regions are summarized in Table 1 and Fig. 1, respectively. The mean time signals for each region were obtained by averaging the fMRI time series across all voxels contained within the VOI, and full

Table 1
Abbreviation and region names used in this study.

#	Abbreviation	Name
1	A1/2	Areas 1 and 2 of cortex
2	A10	Area 10 of cortex
3	A11	Area 11 of cortex
4	A19DI	Area 19 of cortex; dorsointermediate part
5	A19M	Area 19 of cortex; medial part
6	A23a	Area 23a of cortex
7	A23b	Area 23b of cortex
8	A23c	Area 23c of cortex
9	A24d	Area 24d of cortex
10	A32	Area 32 of cortex
11	A32V	Area 32 of cortex; ventral part
12	A3a	Area 3a of cortex (primary somatosensory)
13	A3b	Area 3b of cortex (primary somatosensory)
14	A45	Area 45 of cortex
15	A46D	Area 46 of cortex; dorsal part
16	A47L	Area 47 (old 12) of cortex; lateral part
17	A4ab	Area 4 of cortex; parts a and b (primary motor)
18	A4c	Area 4 of cortex; part c (primary motor)
19	A6DC	Area 6 of cortex; dorsocaudal part
20	A6DR	Area 6 of cortex; dorsorostral part
21	A6M	Area 6 of cortex; medial (supplementary motor) part
22	A6Va	Area 6 of cortex; ventral; part a
23	A8aD	Area 8a of cortex; dorsal part
24	A8aV	Area 8a of cortex; ventral part
25	A8b	Area 8b of cortex
26	A8C	Area 8 of cortex; caudal part
27	A9	Area 9 of cortex
28	AIP	Anterior intraparietal area of cortex
29	AuA1	Auditory cortex; primary area
30	AuCM	Auditory cortex; caudomedial area
31	AuCPB	Auditory cortex; caudal parabelt area
32	AuML	Auditory cortex; middle lateral area
33	AuRT	Auditory cortex; rostrotemporal part
34	LIP	Lateral intraparietal area of cortex
35	MIP	Medial intraparietal area of cortex
36	MST	Medial superior temporal area of cortex
37	OPt	Occipito-parietal transitional area of cortex
38	PE	Parietal area PE
39	PEC	Parietal area PE; caudal part
40	PF	Parietal area PF
41	PFG	Parietal area PFG
42	PG	Parietal area PG
43	PGM	Parietal area PG; medial part
44	PGa_IPa	Parietal areas PGa and IPa
45	S2E	Secondary somatosensory cortex; external part
46	TE3	Temporal area TE3
47	TEO	Temporal area TE; occipital part
48	TPO	Temporo-parieto-occipital association area
49	V1	Visual area 1
50	V2	Visual area 2
51	V3A	Visual area 3A (dorsoanterior area)
52	V4	Visual area 4 (ventrolatereral anterior area)
53	V4T	Visual area 4; transitional part
54	V5	Visual area 5 (middle temporal area)
55	V6	Visual area 6 (dorsomedial area)

correlation coefficients between all regions were then calculated. Finally, FC values in only the 55 cortical regions corresponding to the tracer datasets were extracted for comparison with CC.

2.4. Marmoset retrograde tracer data

Marmoset tracer-based connectivity data is openly available from the Marmoset Brain Connectivity Atlas website (www.marmosetbrain.org) (Majka et al., 2016). Briefly, the weighted and directed connectivity matrix obtained using monosynaptic fluorescent retrograde tracers consists of 116 (source) × 55 (target) areas in the Paxinos Atlas of 116 cortical areas. The fraction of extrinsic labeled neurons (FLNe), the fraction of labeled neurons in a source area relative to the total number of labeled neurons extrinsic to the injected area, can be obtained from the website.

Using these data, we first extracted the complete datasets of both sources and targets (i.e., 55 × 55 matrix), and then symmetrization via mean (i.e., $(DC_{i,j} + DC_{j,i})/2$) was performed to compare FC which has no directional information; where $DC_{i,j}$ denotes direct connection values (FLNe values) of source area index i and injected target area index j. Finally, SC in this study was defined as this average value in logarithmic ($\log_{10}$) units; within-area (area-to-self) connections were not considered.

2.5. Comparison of FC with CC

Both connectivity data were imported into MATLAB (The Mathworks, Natick, MA), and the connectivity matrices of CC and FC were created to visually compare FC with CC. To evaluate overall relationship between CC and FC, Pearson correlation coefficients were calculated. For this calculation, only non-zero CC values were considered (i.e., all false positives and true negatives were excluded from the analysis). To evaluate the area-dependency of FC, we also obtained the Pearson correlation coefficients between CC and FC at each seed region. Additionally, we calculated the Euclidean distance among VOIs to determine the effect of distance on the correlation between CC and FC. We then controlled for the distance between VOIs using MATLAB's "partialcorr" function.

2.6. Detection performance of FC

To assess the quality of our RS-fMRI datasets, we evaluated the detection ability of FC estimated by full correlation coefficient for CC in a binary fashion. The receiver operating characteristic (ROC) curves, sensitivity, and specificity were used to measure the capacity of RS-fMRI. If the CC value was not negative infinity (i.e., FLNe≠0), this connection was considered to be a true connection. For FC, on the other hand, we set cut off values from −0.5 to 1 and a FC value greater than the cut off value was considered to be a predicted connection from FC. The area under the curve (AUC) in ROC curves quantifies the classifier's accuracy. A value of 1 indicates perfect prediction of CC, while a value of 0.5 is chance level.

3. Results

3.1. Comparison of FC with CC

The FC matrix based on the Paxinos Atlas (139 VOIs) was calculated and FC values in only the 55 cortical regions corresponding to the tracer datasets were extracted and compared with CC and Euclidean distance (Fig. 2A, B and 2C). The FC matrix was visually in good agreement with the matrices of CC and inverse Euclidean distance. The scatter plots between FC and CC against inverse distance in the 55 VOIs are shown in Fig. 3A an 3B, respectively. Both FC and CC significantly increased with the increase in the inversed distance between those regions (FC = 0.18 × inverse Euclidean distance - 0.055, r = 0.73, $p < 1.0 \times 10^{-183}$; CC = 5.3 × inverse Euclidean distance - 3.5, r = 0.54, $p < 1.0 \times 10^{-83}$). Fig. 3C shows the scatter plots between CC and FC. The FC values were highly correlated with CC values calculated by retrograde tracers (Fig. 3C; FC = 0.13 × CC + 0.58, r = 0.52, $p < 1.0 \times 10^{-76}$), but the slopes of these correlations were different, varying around CC of −3 (FC = 0.059 × CC + 0.33, r = 0.17, $p < 1.0 \times 10^{-3}$ for −6 ≦ CC ≦ −3; FC = 0.27 × CC + 0.83, r = 0.58, $p < 1.0 \times 10^{-60}$ for −3 < CC < 0). Additionally, when the distance between those regions was short, the correlation between CC and FC was strong, while the distance was long, the correlation was weak (FC = 0.12 × CC + 0.78, r = 0.45, $p < 1.0 \times 10^{-11}$ for distance < 5 mm; FC = 0.063 × CC + 0.42, r = 0.29, $p < 1.0 \times 10^{-9}$ for 5 mm < distance < 10 mm; FC = 0.029 × CC + 0.15, r = 0.17, $p < 1.0 \times 10^{-2}$ for 10 mm < distance < 15 mm; FC = −0.0053 × CC - 0.022, r = −0.031, p = 0.70 for distance > 15 mm).

3.2. Regional differences in the relationship between CC and FC

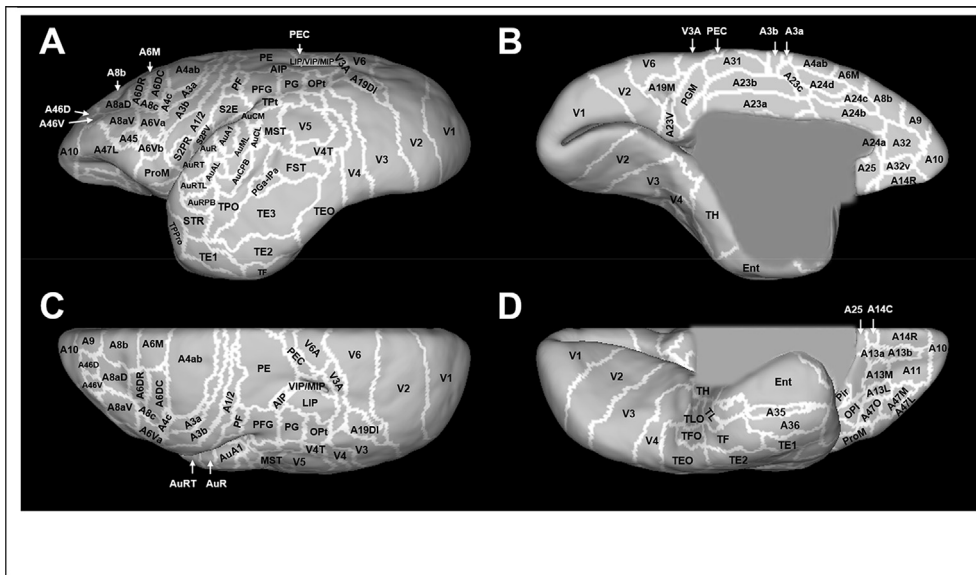To evaluate the regional differences of the reliability of FC, we

Fig. 1. Cytoarchitectonic borders based on the Paxinos atlas (Liu et al., 2018) in lateral (A), medial (B), dorsal (C) and ventral (D) views. Abbreviations used in this study were summarized in Table 1.
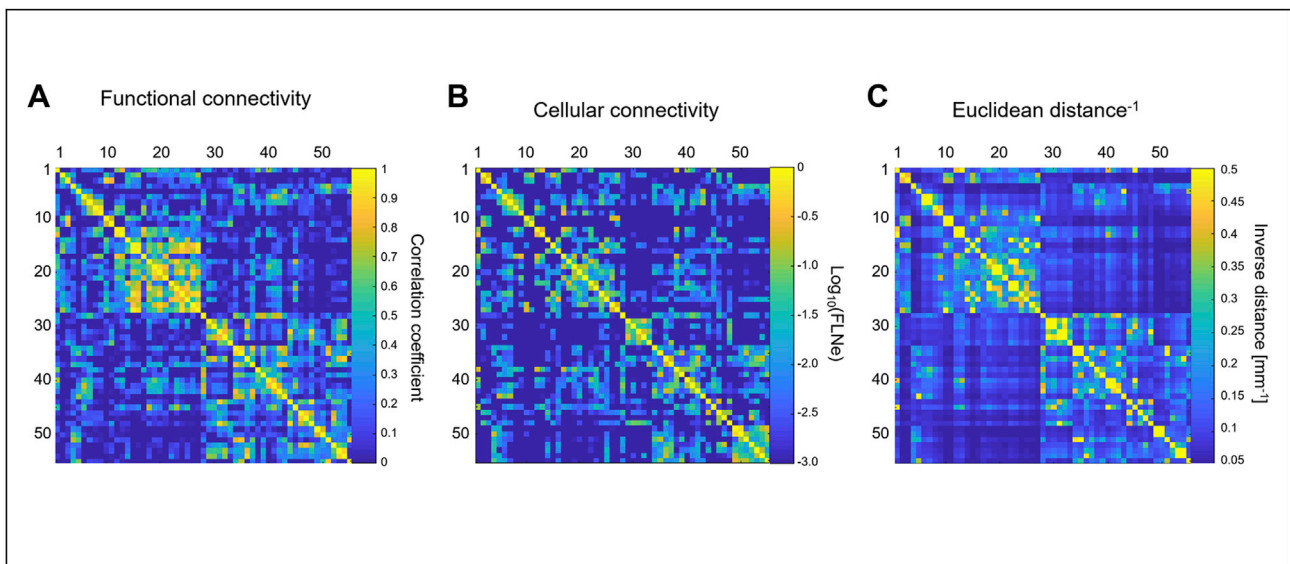

Fig. 2. Matrices of (A) functional connectivity, (B) cellular connectivity, and (C) Euclidean distance. The matrices consist of 55 regions (see Table 1 for labels and ordering of regions #).
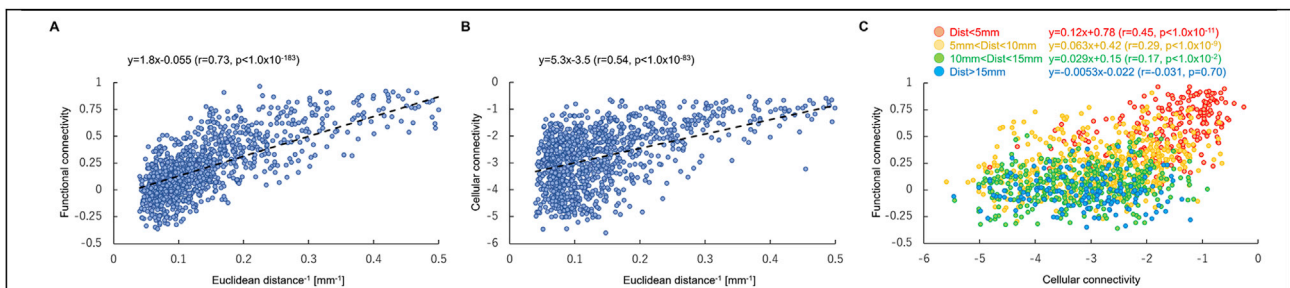

Fig. 3. (A) Scatter plots of functional connectivity (FC) and (B) cellular connectivity (CC) against inverse Euclidean distance. Dashed lines indicate the regression lines between Euclidean distance and connectivity. (C) Scatter plots of FC against CC. Color circles indicate the distance between two regions (red: distance < 5 mm; yellow: 5 mm < distance < 10 mm; green: 10 mm < distance < 15 mm; blue: distance > 15 mm).

obtained the relationship between CC and FC for each seed region (Figs. 4 and 5). Pearson correlation coefficients between CC and FC varied markedly across seed regions and ranged from 0.19 (A23a) to 0.83 (A1/ 2) (Fig. 4A). The average and standard deviation (s.d.) of the correlation coefficients were 0.54 ± 0.15. Fig. 5 shows examples of FC maps with CC maps. Some areas like 23c and 1/2 exhibited strong correlations between FC and CC (Fig. 5A and B), other areas like 11 and 6DC showed intermediate correlations between full FC and CC (Fig. 5C and D), and some areas like 45 and 23a exhibited weak correlations between full FC and CC (Fig. 5E and F). Area 23c was structurally connected to sensorimotor areas (1/2, 3a, 3b, and 4 ab), parietal areas (PE and PFG), and cingulate areas (23a, 23b, and 24d). The FC maps exhibited patterns similar to the CC maps (Fig. 5A). This tendency was also consistent when the seed region was area 1/2 (Fig. 5B). In contrast, areas 11, 6DC, 45 and 23a were sparsely connected to various cortical regions in CC maps, but the distributions of FC maps were restricted to the specific regions (Fig. 5C, D, 5E and 5F). To regress out the effect of the distance between two brain regions, we also calculated the Pearson correlation coefficients between CC and FC for each seed region, while controlling for the distance between VOIs (Fig. 4B). Pearson correlation coefficients between CC and FC still varied markedly across seed regions and ranged from -0.10 (A23b) to 0.67 (A19DI). The average of the correlation coefficient were lower than those before controlling for the effect of the distance (0.28 ± 0.19; $p < 1.0 \times 10^{-17}$; paired t-test), but some regions have strong correlations.

3.3. Detection performance of FC for CC

To assess the quality of our RS-fMRI datasets, we evaluated the detection ability of FC estimated by full correlation coefficient for CC in a binary fashion. The ROC curve, sensitivity and specificity are shown in Fig. 6. The AUC in ROC curves quantifies the classifier's accuracy. A value of 1 indicates perfect prediction of CC, while a value of 0.5 is chance level. The AUC in the ROC curve was 0.72, which is similar to that for a recent study which compared diffusion tractography with tracers in postmortem macaque monkeys (AUC = 0.71–0.72) (Donahue et al., 2016). The intersection between sensitivity and specificity curves corresponds to a FC cut-off value of 0.068, which offers a balanced compromise between maximizing true positives and minimizing false positives.

4. Discussion

RS-fMRI is widely used to assess how strongly different brain areas are connected (Damoiseaux and Greicius, 2009; Fox and Raichle, 2007;
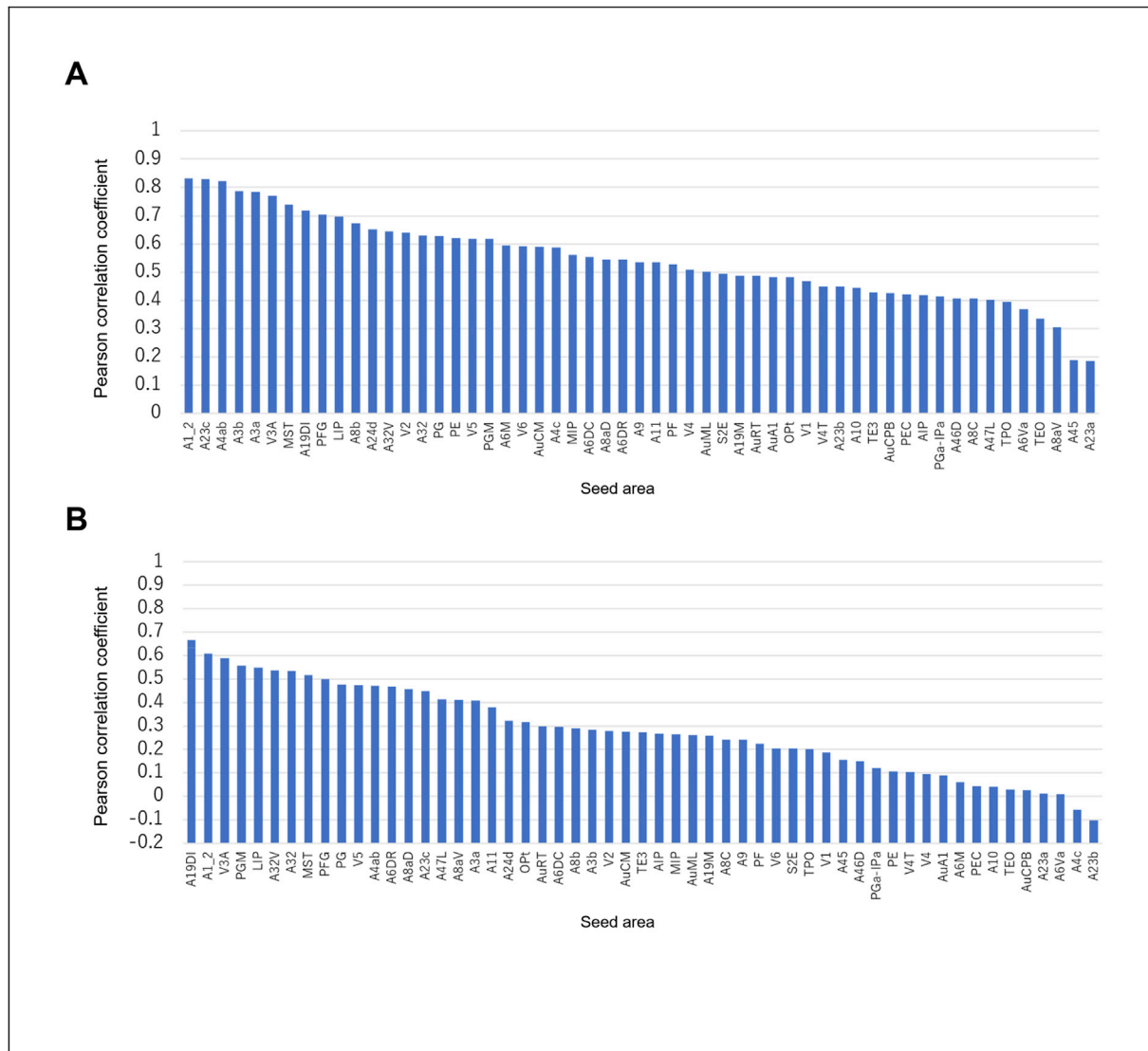
Fig. 4. Pearson correlation coefficients between functional connectivity (FC) and cellular connectivity (CC) in each seed region, before (A) and after (B) controlling the effects of the distance between two brain regions.
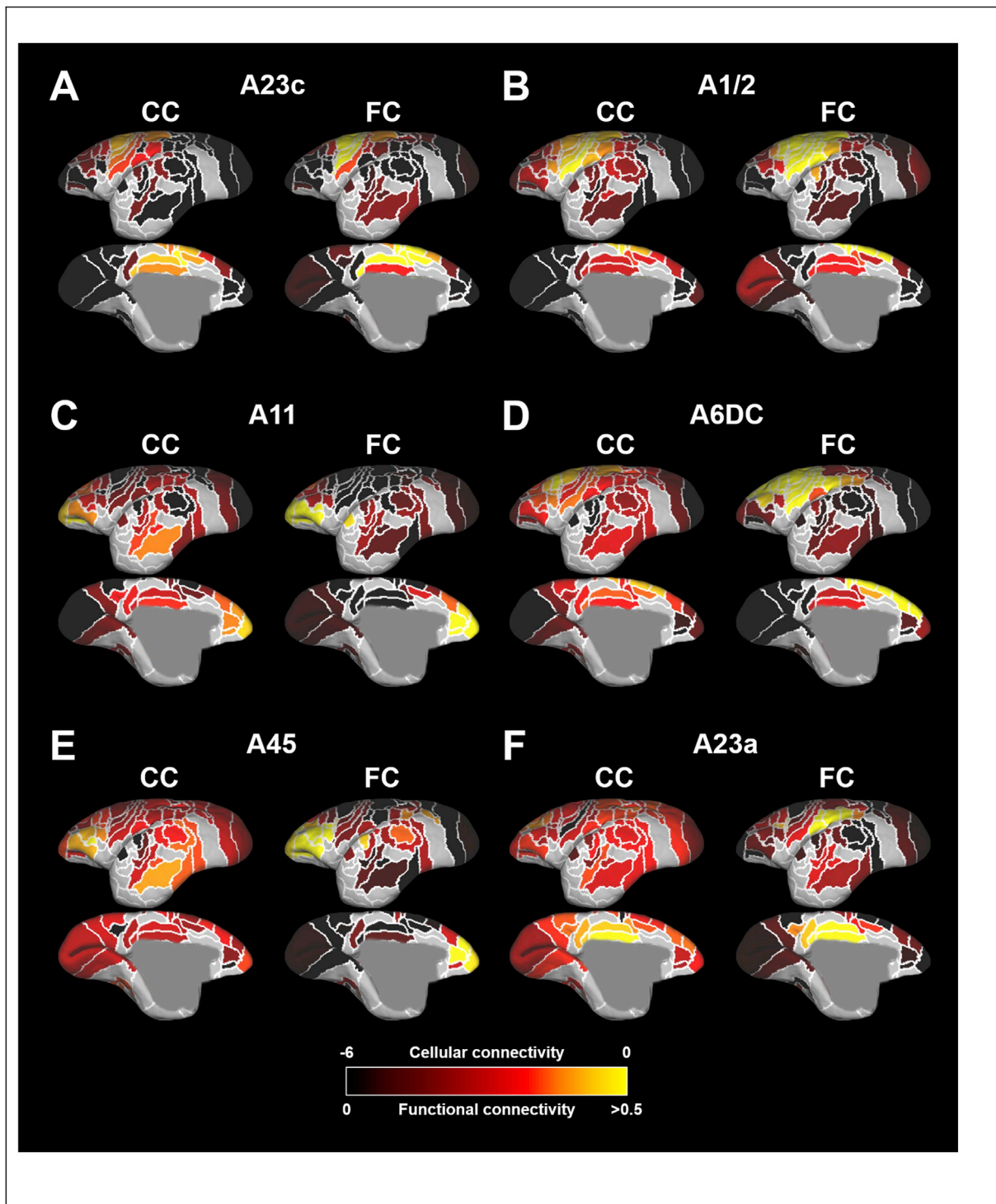
Fig. 5. Representative cellular (CC) and functional connectivity (FC) on the surface map. Seed regions were A23c (A) and A1/2 (B) for the examples of strong correlations, A11 (C) and A6DC (D) for the examples of intermediate correlations, and A45 (E) and 23a (F) for the examples of weak correlations, respectively.

Johnston et al., 2008; Park and Friston, 2013; Smith et al., 2013; Sporns, 2013). However, it has yet to be quantified how accurately FC reflects CC. In this study, we quantified FC in marmosets using RS-fMRI and addressed these long-standing questions about the relationship between FC and CC. Our main findings are: (1) overall FC was highly correlated with tracer-based CC ($r = 0.52$), but correlation coefficients between FC and CC varied remarkably across seed regions; (2) the strength of FC decreases with increase in the distance between two regions; (3) correlation coefficients after regressing out the effect of the distance between

two regions still varied across seed regions, but some regions have strong correlations. These findings suggest that FC reflects the strength of monosynaptic pathway, although FC is strongly affected by the distance between regions.

From the comparison of FC with Euclidean distance between brain regions, we found that the strength of FC decreases with the distance between regions ($r = 0.73$). We also found that when the distance between two regions is short, the correlation between CC and FC is strong, while when the distance between two regions is long, the correlation is
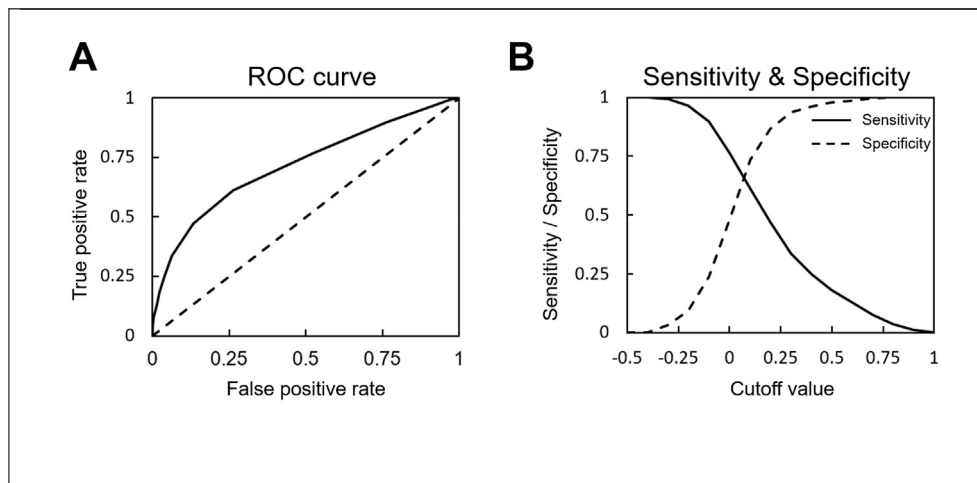
Fig. 6. Detection performance of full correlation-based functional connectivity (FC) for cellular connectivity (CC). The area under the curve (AUC) of the receiver operating characteristic (ROC) (A) is 0.72. The dashed line shows the chance level. Fig. (B) shows sensitivity and specificity. The intersection between sensitivity and specificity curves corresponded to a FC cut-off value of 0.068.

weak. These findings are consistent with a previous study using RS-fMRI and diffusion tractography in humans (Honey et al., 2009). It is already known that FC between brain regions is affected by the distance between brain regions (Salvador et al., 2005), and this effect could result from distance-dependent factors, including (1) activation spread along the surface of the cortex via local circuitry, and (2) spatial blurring of the BOLD signal because of vascular drainage (Honey et al., 2009; Rubino et al., 2006). These factors might artifactually increase the correlation between FC and tracer-based CC. In fact, when seed regions were areas 1/2 and 23c, these regions were anatomically connected to regions close to the seed regions and FC maps were in good agreement with CC maps. To overcome this problem, we also calculated the Pearson correlation coefficients between CC and FC for each seed region, while controlling for the Euclidean distance between two regions. The correlation coefficients still varied across seed regions, but some regions had high correlations between FC and CC. These findings suggest that FC reflects the strength of monosynaptic pathways, and the variation of correlation coefficients reflect the relative contributions of monosynaptic and polysynaptic pathways. Because FC reflects not only direct (monosynaptic) connection but also indirect (polysynaptic) connection while CC reflects only direct connections, the high correlation areas indicate those regions that have a lot of monosynaptic connections like a hub region. Indeed, it is known that areas 8aD, PG, LIP, and PGM play important roles as hubs (Ghahremani et al., 2016; Liu et al., 2019), and FC in these regions were highly correlated with CC. The low correlation areas may reflect the effect of polysynaptic connection on FC, but testing this idea was beyond the scope of the present study because cellular connectivity data is not available for all regions. To assess the quality of our RS-fMRI datasets, we evaluated the detection ability of FC estimated by full correlation coefficients for CC in a binary fashion. The AUC in the ROC curve was 0.72, which was similar to that for recent diffusion tractography versus tracers in postmortem macaque monkeys (AUC = 0.71–0.72) (Donahue et al., 2016). This result indicates that this RS-fMRI dataset has reasonably high quality to reflect CC. The intersection between sensitivity and specificity curves corresponded to a FC cut-off value of 0.068, which offers a balanced compromise between maximizing true positives and minimizing false positives. These performance evaluations will be useful for assessing the quality of future RS-fMRI data in marmosets.

In this study, we aimed to compare FC with tracer-based CC anatomical connections because it is currently considered as a gold standard technique to detect the direct anatomical connections; however, even this technique has methodological limitations. Repeated tracer injections into the same area often yield different estimated connection values (Markov et al., 2011), presumably reflecting a combination of

individual variability in connection weight, differences of types of fluorescent tracers, statistical fluctuation and technical limitations. The variability in the connections of different parts of the same cytoarchitectural area (Paxinos et al., 2012) is also one of the factors. For example, the connections of the foveal representation of cortical areas are very different from those of the peripheral representation (Palmer and Rosa, 2006). The connections of the representations of the face, hand and legs in primary motor cortex are also different. Another potential limitation is that we scanned the marmosets under 1.5% isoflurane anesthesia to avoid the effects of motion and physiological stress, even though it remains unclear how isoflurane affects FC in marmosets. However, recent fMRI studies with isoflurane anesthesia demonstrated clear functional boundaries in anterior cingulate cortex and lateral prefrontal cortex (Schaeffer et al., 2019a, 2019b), and global functional networks in marmosets under isoflurane anesthesia (Ghahremani et al., 2016). In a previous macaque study (Hutchison et al., 2014), our group suggested the use of up to 1.5% isoflurane anesthesia was acceptable because the spatial structure of the functional network was preserved. These findings show that 1.5% isoflurane anesthesia reveals functional networks in marmosets.

RS-fMRI in marmosets is recently expected as a preclinical model to evaluate the brain mechanisms underlying neuropsychiatric disorders, because of its characteristics such as well-developed frontal lobe (Okano and Mitra, 2015) and the recent developments of transgenic marmosets (Park et al., 2016; Sasaki et al., 2009; Tomioka et al., 2017). Overall, our results showed that FC obtained by RS-fMRI in marmosets reflects the strength of tracer-based CC, but we also demonstrated that correlation coefficients varied remarkably across seed region. Although what are other factors affecting FC is an important question for future inquiry, our findings reveal the feasibility of FC to infer how strongly different brains are connected and provide a critical foundation for future work that aims to test FC changes in marmoset models as an alternative to human.

Author contribution

Y.H., D.J.S. and S.E. designed research; Y.H., D.J.S., K.M.G., L.K.H., J.C.C., J.S.G. and S.E. performed research; Y.H. and D.J.S. analyzed data; Y.H. wrote the paper; and Y.H., D.J.S., K.M.G., L.K.H., J.C.C., J.S.G., R.S.M. and S.E. edited the paper.

Declaration of competing interest

The authors declare no conflict of interest.

Acknowledgement

References

Abe, H., Tani, T., Mashiko, H., Kitamura, N., Hayami, T., Watanabe, S., Sakai, K., Suzuki, W., Mizukami, H., Watakabe, A., Yamamori, T., Ichinohe, N., 2018. Axonal projections from the middle temporal area in the common marmoset. Front. Neuroanat. 12, 89. https://doi.org/10.3389/fnana.2018.00089.

Burman, K.J., Bakola, S., Richardson, K.E., Yu, H.-H., Reser, D.H., Rosa, M.G.P., 2015. Cortical and thalamic projections to cytoarchitectural areas 6Va and 8C of the marmoset monkey: connectionally distinct subdivisions of the lateral premotor cortex: connections of marmoset lateral premotor cortex. J. Comp. Neurol. 523, 1222–1247. https://doi.org/10.1002/cne.23734.

Damoiseaux, J.S., Greicius, M.D., 2009. Greater than the sum of its parts: a review of studies combining structural connectivity and resting-state functional connectivity. Brain Struct. Funct. 213, 525–533. https://doi.org/10.1007/s00429-009-0208-6.

Donahue, C.J., Sotiropoulos, S.N., Jbabdi, S., Hernandez-Fernandez, M., Behrens, T.E., Dyrby, T.B., Coalson, T., Kennedy, H., Knoblauch, K., Van Essen, D.C., Glasser, M.F., 2016. Using diffusion tractography to predict cortical connection strength and distance: a quantitative comparison with tracers in the monkey. J. Neurosci. 36, 6758–6770. https://doi.org/10.1523/JNEUROSCI.0493-16.2016.

Fox, M.D., Raichle, M.E., 2007. Spontaneous fluctuations in brain activity observed with functional magnetic resonance imaging. Nat. Rev. Neurosci. 8, 700–711. https://doi.org/10.1038/nrn2201.

Ghahremani, M., Hutchison, R.M., Menon, R.S., Everling, S., 2016. Frontoparietal functional connectivity in the common marmoset. Cerebr. Cortex 27, 3890–3905. https://doi.org/10.1093/cercor/bhw198.

Gilbert, K.M., Gati, J.S., Klassen, L.M., Zeman, P., Schaeffer, D.J., Everling, S., Menon, R.S., 2017. A geometrically adjustable receive array for imaging marmoset cohorts. Neuroimage 156, 78–86. https://doi.org/10.1016/j.neuroimage.2017.05.013.

Greicius, M.D., Srivastava, G., Reiss, A.L., Menon, V., 2004. Default-mode network activity distinguishes Alzheimer's disease from healthy aging: evidence from functional MRI. Proc. Natl. Acad. Sci. U.S.A. 101, 4637–4642. https://doi.org/10.1073/pnas.0308627101.

Greicius, M.D., Supekar, K., Menon, V., Dougherty, R.F., 2009. Resting-state functional connectivity reflects structural connectivity in the default mode network. Cerebr. Cortex 19, 72–78. https://doi.org/10.1093/cercor/bhn059.

Griffanti, L., Douaud, G., Bijsterbosch, J., Evangelisti, S., Alfaro-Almagro, F., Glasser, M.F., Duff, E.P., Fitzgibbon, S., Westphal, R., Carone, D., Beckmann, C.F., Smith, S.M., 2017. Hand classification of fMRI ICA noise components. Neuroimage 154, 188–205. https://doi.org/10.1016/j.neuroimage.2016.12.036.

Hagmann, P., Cammoun, L., Gigandet, X., Meuli, R., Honey, C.J., Wedeen, V.J., Sporns, O., 2008. Mapping the structural core of human cerebral cortex. PLoS Biol. 6, e159. https://doi.org/10.1371/journal.pbio.0060159.

Helmich, R.C., Derikx, L.C., Bakker, M., Scheeringa, R., Bloem, B.R., Toni, I., 2010. Spatial remapping of cortico-striatal connectivity in Parkinson's disease. Cerebr. Cortex 20, 1175–1186. https://doi.org/10.1093/cercor/bhp178.

Honey, C.J., Sporns, O., Cammoun, L., Gigandet, X., Thiran, J.P., Meuli, R., Hagmann, P., 2009. Predicting human resting-state functional connectivity from structural connectivity. Proc. Natl. Acad. Sci. 106, 2035–2040. https://doi.org/10.1073/pnas.0811168106.

Hutchison, R.M., Hutchison, M., Manning, K.Y., Menon, R.S., Everling, S., 2014. Isoflurane induces dose-dependent alterations in the cortical connectivity profiles and dynamic properties of the brain's functional architecture: dose-Dependent Isoflurane Effects. Hum. Brain Mapp. 35, 5754–5775. https://doi.org/10.1002/hbm.22583.

Jbabdi, S., Johansen-Berg, H., 2011. Tractography: where do we go from here? Brain Connect. 1, 169–183. https://doi.org/10.1089/brain.2011.0033.

Jbabdi, S., Sotiropoulos, S.N., Haber, S.N., Van Essen, D.C., Behrens, T.E., 2015. Measuring macroscopic brain connections in vivo. Nat. Neurosci. 18, 1546–1555. https://doi.org/10.1038/nn.4134.

Johnston, J.M., Vaishnavi, S.N., Smyth, M.D., Zhang, D., He, B.J., Zempel, J.M., Shimony, J.S., Snyder, A.Z., Raichle, M.E., 2008. Loss of resting interhemispheric functional connectivity after complete section of the corpus callosum. J. Neurosci. 28, 6453–6458. https://doi.org/10.1523/JNEUROSCI.0573-08.2008.

Koch, M.A., Norris, D.G., Hund-Georgiadis, M., 2002. An investigation of functional and anatomical connectivity using magnetic resonance imaging. Neuroimage 16, 241–250. https://doi.org/10.1006/nimg.2001.1052.

Li, X., Morgan, P.S., Ashburner, J., Smith, J., Rorden, C., 2016. The first step for neuroimaging data analysis: DICOM to NIfTI conversion. J. Neurosci. Methods 264, 47–56. https://doi.org/10.1016/j.jneumeth.2016.03.001.

Liu, C., Ye, F.Q., Yen, C.C.-C., Newman, J.D., Glen, D., Leopold, D.A., Silva, A.C., 2018. A digital 3D atlas of the marmoset brain based on multi-modal MRI. Neuroimage 169, 106–116. https://doi.org/10.1016/j.neuroimage.2017.12.004.

Liu, C., Yen, C.C.-C., Szczupak, D., Ye, F.Q., Leopold, D.A., Silva, A.C., 2019. Anatomical and functional investigation of the marmoset default mode network. Nat. Commun. 10, 1975. https://doi.org/10.1038/s41467-019-09813-7.

Majka, P., Chaplin, T.A., Yu, H.-H., Tolpygo, A., Mitra, P.P., Wójcik, D.K., Rosa, M.G.P., 2016. Towards a comprehensive atlas of cortical connections in a primate brain: mapping tracer injection studies of the common marmoset into a reference digital template: atlas of primate brain cortical connections. J. Comp. Neurol. 524, 2161–2181. https://doi.org/10.1002/cne.24023.

Marcus, D.S., Harwell, J., Olsen, T., Hodge, M., Glasser, M.F., Prior, F., Jenkinson, M., Laumann, T., Curtiss, S.W., Van Essen, D.C., 2011. Informatics and data mining tools and strategies for the human connectome project. Front. Neuroinf. 5. https://doi.org/10.3389/fninf.2011.00004.

Markov, N.T., Ercsey-Ravasz, M.M., Ribeiro Gomes, A.R., Lamy, C., Magrou, L., Vezoli, J., Misery, P., Falchier, A., Quilodran, R., Gariel, M.A., Sallet, J., Gamanut, R., Huissoud, C., Clavagnier, S., Giroud, P., Sappey-Marinier, D., Barone, P., Dehay, C., Toroczkai, Z., Knoblauch, K., Van Essen, D.C., Kennedy, H., 2014. A weighted and directed interareal connectivity matrix for macaque cerebral cortex. Cerebr. Cortex 24, 17–36. https://doi.org/10.1093/cercor/bhs270.

Markov, N.T., Misery, P., Falchier, A., Lamy, C., Vezoli, J., Quilodran, R., Gariel, M.A., Giroud, P., Ercsey-Ravasz, M., Pilaz, L.J., Huissoud, C., Barone, P., Dehay, C., Toroczkai, Z., Van Essen, D.C., Kennedy, H., Knoblauch, K., 2011. Weight consistency specifies regularities of macaque cortical networks. Cerebr. Cortex 21, 1254–1272. https://doi.org/10.1093/cercor/bhq201.

Miranda-Dominguez, O., Mills, B.D., Grayson, D., Woodall, A., Grant, K.A., Kroenke, C.D., Fair, D.A., 2014. Bridging the gap between the human and macaque connectome: a quantitative comparison of global interspecies structure-function relationships and network topology. J. Neurosci. 34, 5552–5563. https://doi.org/10.1523/JNEUROSCI.4229-13.2014.

Okano, H., Mitra, P., 2015. Brain-mapping projects using the common marmoset. Neurosci. Res. 93, 3–7. https://doi.org/10.1016/j.neures.2014.08.014.

Park, H.-J., Friston, K., 2013. Structural and functional brain networks: from connections to cognition. Science 342, 1238411–1238411. https://doi.org/10.1126/science.1238411.

Park, J.E., Zhang, X.F., Choi, S.-H., Okahara, J., Sasaki, E., Silva, A.C., 2016. Generation of transgenic marmosets expressing genetically encoded calcium indicators. Sci. Rep. 6. https://doi.org/10.1038/srep34931.

Palmer, S.M., Rosa, M.G.P., 2006. A distinct anatomical network of cortical areas for analysis of motion in far peripheral vision. Eur. J. Neurosci. 24, 2389–2405. https://doi.org/10.1111/j.1460-9568.2006.05113.x.

Paxinos, G., Watson, C., Petrides, M., Rosa, M., Tokuno, H., 2012. The Marmoset Brain in Stereotaxic Coordinates. Academic Press. http://hdl.handle.net/20.500.11937/40725.

Peterson, J., Chaddock, R., Dalrymple, B., Van Sas, F., Gilbert, K.M., Klassen, L.M., Gati, J.S., Handler, W.B., Chronik, B.A., 2018. Development of a gradient and shim insert system for marmoset imaging at 9.4 T. In: Proceedings of the 26th Annual Meeting ISMRM, p. 4421. Paris, France. https://www.scopus.com/home.uri.

Pozzi, L., Hodgson, J.A., Burrell, A.S., Sterner, K.N., Raaum, R.L., Disotell, T.R., 2014. Primate phylogenetic relationships and divergence dates inferred from complete mitochondrial genomes. Mol. Phylogenetics Evol. 75, 165–183. https://doi.org/10.1016/j.ympev.2014.02.023.

Reser, D.H., Burman, K.J., Yu, H.-H., Chaplin, T.A., Richardson, K.E., Worthy, K.H., Rosa, M.G.P., 2013. Contrasting patterns of cortical input to architectural subdivisions of the area 8 complex: a retrograde tracing study in marmoset monkeys. Cerebr. Cortex 23, 1901–1922. https://doi.org/10.1093/cercor/bhs177.

Reser, D.H., Majka, P., Snell, S., Chan, J.M.H., Watkins, K., Worthy, K., Quiroga, M.D.M., Rosa, M.G.P., 2017. Topography of claustrum and insula projections to medial prefrontal and anterior cingulate cortices of the common marmoset (Callithrix jacchus): claustrum and insula projections to marmoset MPFC and ACC. J. Comp. Neurol. 525, 1421–1441. https://doi.org/10.1002/cne.24009.

Rombouts, S.A.R.B., Barkhof, F., Goekoop, R., Stam, C.J., Scheltens, P., 2005. Altered resting state networks in mild cognitive impairment and mild Alzheimer's disease: an fMRI study. Hum. Brain Mapp. 26, 231–239. https://doi.org/10.1002/hbm.20160.

Rubino, D., Robbins, K.A., Hatsopoulos, N.G., 2006. Propagating waves mediate information transfer in the motor cortex. Nat. Neurosci. 9, 1549–1557. https://doi.org/10.1038/nn1802.

Rytty, R., Nikkinen, J., Paavola, L., Abou Elseoud, A., Moilanen, V., Visuri, A., Tervonen, O., Renton, A.E., Traynor, B.J., Kiviniemi, V., Remes, A.M., 2013. GroupICA dual regression analysis of resting state networks in a behavioral variant of frontotemporal dementia. Front. Hum. Neurosci. 7. https://doi.org/10.3389/fnhum.2013.00461.

Salvador, R., Suckling, J., Coleman, M.R., Pickard, J.D., Menon, D., Bullmore, E., 2005. Neurophysiological architecture of functional magnetic resonance images of human brain. Cerebr. Cortex 15, 1332–1342. https://doi.org/10.1093/cercor/bhi016.

Sasaki, E., Suemizu, H., Shimada, A., Hanazawa, K., Oiwa, R., Kamioka, M., Tomioka, I., Sotomaru, Y., Hirakawa, R., Eto, T., Shiozawa, S., Maeda, T., Ito, M., Ito, R., Kito, C., Yagihashi, C., Kawai, K., Miyoshi, H., Tanioka, Y., Tamaoki, N., Habu, S., Okano, H., Nomura, T., 2009. Generation of transgenic non-human primates with germline transmission. Nature 459, 523–527. https://doi.org/10.1038/nature08090.

Schaeffer, D.J., Gilbert, K.M., Gati, J.S., Menon, R.S., Everling, S., 2019a. Intrinsic functional boundaries of lateral frontal cortex in the common marmoset monkey. J. Neurosci. 39, 1020–1029. https://doi.org/10.1523/JNEUROSCI.2595-18.2018.

Schaeffer, D.J., Gilbert, K.M., Ghahremani, M., Gati, J.S., Menon, R.S., Everling, S., 2019b. Intrinsic functional clustering of anterior cingulate cortex in the common marmoset. Neuroimage 186, 301–307. https://doi.org/10.1016/j.neuroimage.2018.11.005.

Schaeffer, D.J., Gilbert, K.M., Hori, Y., Gati, J.S., Menon, R.S., Everling, S., 2019c. Integrated radio frequency array and animal holder design for minimizing head motion during awake marmoset functional magnetic resonance imaging. Neuroimage 193, 126–138. https://doi.org/10.1016/j.neuroimage.2019.03.023.

Shen, K., Bezgin, G., Hutchison, R.M., Gati, J.S., Menon, R.S., Everling, S., McIntosh, A.R., 2012. Information processing architecture of functionally defined clusters in the macaque cortex. J. Neurosci. 32, 17465–17476. https://doi.org/10.1523/JNEUROSCI.2709-12.2012.

Shen, K., Goulas, A., Grayson, D.S., Eusebio, J., Gati, J.S., Menon, R.S., McIntosh, A.R., Everling, S., 2019. Exploring the limits of network topology estimation using diffusion-based tractography and tracer studies in the macaque cortex. Neuroimage 191, 81–92. https://doi.org/10.1016/j.neuroimage.2019.02.018.

Skudlarski, P., Jagannathan, K., Calhoun, V.D., Hampson, M., Skudlarska, B.A., Pearlson, G., 2008. Measuring brain connectivity: diffusion tensor imaging validates resting state temporal correlations. Neuroimage 43, 554–561. https://doi.org/10.1016/j.neuroimage.2008.07.063.

Smith, S.M., Beckmann, C.F., Andersson, J., Auerbach, E.J., Bijsterbosch, J., Douaud, G., Duff, E., Feinberg, D.A., Griffanti, L., Harms, M.P., Kelly, M., Laumann, T., Miller, K.L., Moeller, S., Petersen, S., Power, J., Salimi-Khorshidi, G., Snyder, A.Z., Vu, A.T., Woolrich, M.W., Xu, J., Yacoub, E., Uğurbil, K., Van Essen, D.C., Glasser, M.F., 2013. Resting-state fMRI in the human connectome project. Neuroimage 80, 144–168. https://doi.org/10.1016/j.neuroimage.2013.05.039.

Smith, S.M., Jenkinson, M., Woolrich, M.W., Beckmann, C.F., Behrens, T.E.J., Johansen-Berg, H., Bannister, P.R., De Luca, M., Drobnjak, I., Flitney, D.E., Niazy, R.K., Saunders, J., Vickers, J., Zhang, Y., De Stefano, N., Brady, J.M., Matthews, P.M., 2004. Advances in functional and structural MR image analysis and implementation as FSL. Neuroimage 23, S208–S219. https://doi.org/10.1016/j.neuroimage.2004.07.051.

Sporns, O., 2013. The human connectome: origins and challenges. Neuroimage 80, 53–61. https://doi.org/10.1016/j.neuroimage.2013.03.023.

Stephan, K.E., Kamper, L., Bozkurt, A., Burns, G.A.P.C., Young, M.P., Kötter, R., 2001. Advanced database methodology for the collation of connectivity data on the macaque brain (CoCoMac). Philos. Trans. Royal Soc. B 356, 1159–1186. https://doi.org/10.1098/rstb.2001.0908.

Swanson, L.W., 1982. The projections of the ventral tegmental area and adjacent regions: a combined fluorescent retrograde tracer and immunofluorescence study in the rat. Brain Res. Bull. 9, 321–353.

Tomioka, I., Nogami, N., Nakatani, T., Owari, K., Fujita, N., Motohashi, H., Takayama, O., Takae, K., Nagai, Y., Seki, K., 2017. Generation of transgenic marmosets using a tetracyclin-inducible transgene expression system as a neurodegenerative disease model. Biol. Reprod. 97, 772–780. https://doi.org/10.1093/biolre/iox129.

Van den Heuvel, M., Mandl, R., Luigjes, J., Hulshoff Pol, H., 2008. Microstructural organization of the cingulum tract and the level of default mode functional connectivity. J. Neurosci. 28, 10844–10851. https://doi.org/10.1523/JNEUROSCI.2964-08.2008.

Van Essen, D.C., Dierker, D.L., 2007. Surface-based and probabilistic atlases of primate cerebral cortex. Neuron 56, 209–225. https://doi.org/10.1016/j.neuron.2007.10.015.

Wang, L., Zang, Y., He, Y., Liang, M., Zhang, X., Tian, L., Wu, T., Jiang, T., Li, K., 2006. Changes in hippocampal connectivity in the early stages of Alzheimer's disease: evidence from resting state fMRI. Neuroimage 31, 496–504. https://doi.org/10.1016/j.neuroimage.2005.12.033.

Warner, C.E., Kwan, W.C., Wright, D., Johnston, L.A., Egan, G.F., Bourne, J.A., 2015. Preservation of vision by the pulvinar following early-life primary visual cortex lesions. Curr. Biol. 25, 424–434. https://doi.org/10.1016/j.cub.2014.12.028.

Wu, T., Wang, L., Chen, Y., Zhao, C., Li, K., Chan, P., 2009. Changes of functional connectivity of the motor network in the resting state in Parkinson's disease. Neurosci. Lett. 460, 6–10. https://doi.org/10.1016/j.neulet.2009.05.046.

Zarei, M., Beckmann, C.F., Binnewijzend, M.A.A., Schoonheim, M.M., Oghabian, M.A., Sanz-Arigita, E.J., Scheltens, P., Matthews, P.M., Barkhof, F., 2013. Functional segmentation of the hippocampus in the healthy human brain and in Alzheimer's disease. Neuroimage 66, 28–35. https://doi.org/10.1016/j.neuroimage.2012.10.071.

Zeater, N., Buzás, P., Dreher, B., Grünert, U., Martin, P.R., 2019. Projections of three subcortical visual centers to marmoset lateral geniculate nucleus. J. Comp. Neurol. 527, 535–545. https://doi.org/10.1002/cne.24390.

Zhou, J., Greicius, M.D., Gennatas, E.D., Growdon, M.E., Jang, J.Y., Rabinovici, G.D., Kramer, J.H., Weiner, M., Miller, B.L., Seeley, W.W., 2010. Divergent network connectivity changes in behavioural variant frontotemporal dementia and Alzheimer's disease. Brain 133, 1352–1367. https://doi.org/10.1093/brain/awq075.